Mechanically Induced Homochirality in Nucleated Enantioselective Polymerization

Celia Blanco,[†] Michael Stich,[‡] and David Hochberg[*,¶]

†*Department of Chemistry and Biochemistry, University of California, Santa Barbara, CA 93106-9510, USA*

‡*Non-linearity and Complexity Research Group, System Analytics Research Institute, School of Engineering and Applied Science, Aston University, B4 7ET Birmingham, UK*

¶*Department of Molecular Evolution, Centro de Astrobiología (CSIC-INTA), Carretera Ajalvir Kilómetro 4, 28850 Torrejón de Ardoz, Madrid, Spain.*

E-mail: hochbergd@cab.inta-csic.es

Abstract

Understanding how biological homochirality may have emerged during chemical evolution remains a challenge for origin of life research. In keeping with this goal, we introduce and solve numerically a kinetic rate equation model of nucleated cooperative enantioselective polymerization in closed systems. The microreversible scheme includes (i) solution phase racemization of the monomers, (ii) linear chain growth by stepwise monomer attachment, in both the nucleation and elongation phases, and (iii) annealing or fusion of homochiral chains. Mechanically induced breakage of the longest chains maintains the system out of equilibrium and drives a breakage-fusion recycling mechanism. Spontaneous mirror symmetry breaking (SMSB) can be achieved starting from small initial enantiomeric excesses due to the intrinsic statistical fluctuations about the idealized racemic composition. The subsequent chiral amplification confirms the

model's capacity for absolute asymmetric synthesis, and without chiral cross-inhibition and without explicit autocatalysis.

Introduction

Biological homochirality of living systems involves large macromolecules, often biopolymers. The origin of homochirality has been much debated, and includes the possibility that the origin of elementary chiral molecules may well be astrophysical.[1] A key question in this context is the relationship of the polymerization process with the emergence of chirality. This question has spurred recent activity devoted to modeling efforts aimed at understanding mirror symmetry breaking and chiral amplification in chiral polymerization of potential relevance to the origin of life. The majority of the kinetic models thus far studied[2–7] are extensions and generalizations of Frank's original paradigmatic scheme[8] which is based on mutual, or chiral inhibition. An early pioneering conceptual model[2] introduced a detailed polymerization process plus the basic elements of enantiomeric cross inhibition as well as a chiral feedback mechanism in which only the largest polymers formed can enhance the production of the chiral monomers from an achiral substrate. Spatial extent and diffusion can be included in such schemes[3] to study the spread and propagation of chiral domains as well as the influence of backround turbulent advection velocity fields. In related models, the polymers may grow to arbitrary lengths and the chiral polymers of all lengths, from the dimer on upwards, can act catalytically in the breakdown of the achiral source into chiral monomers.[5] The role of external white noise on such polymerization networks including spatial extent has also been explored[6,7] to model random environmental disturbances. Another variation on this theme[9] gives rise to homochiral states in dimerization, but without invoking the enantiomeric cross inhibition, allowing instead for reversibility in all the reaction steps. This requires an open flow, which is the needed element of irreversibility for achieving non-equilibrium steady states. The important role of microscopic reversibility in chiral asymmetry has also been

investigated in detail for some basic non-polymerization models.[10,11]

These polymerization models are defined for *open flow* systems which exchange matter and energy with the environment. A constant (unlimited) source of achiral precursor is typically assumed. As a consequence, the homochiral chains can grow to infinite length and unbounded mass. By contrast, typical laboratory experimental procedures are carried out in *closed and spatially bounded* reaction domains and are initiated in far-from equilibrium states.[12–19] Moreover, unbounded polymerization is prevented by entropic effects which imply a finite maximum chain length that depends on temperature. It is important to have models compatible with such experimentally realistic boundary and initial conditions[20–23] and in conformance with thermodynamic constraints. The most immediate consequences are that polymer chains can grow to a finite maximum length, and that the total system mass is constant.

Reaction networks and system architectures, are important elements to have in mind in the design of experiments that might lead to absolute asymmetric synthesis or even to temporary mirror symmetry breaking (kinetically controlled chiral excursions[24]). In this paper, we introduce and analyze a kinetic scheme involving (i) a racemizing pair of enantiomeric monomers, (ii) the assembly of these monomers into supramolecular fibers or linear architectures, (iii) binary fiber annealing and fragmentation, and (iv) mechanically induced breakage of the longer fibers into smaller ones. This modeling is useful in order to acquire deeper chemical/physical insights into the basic processes involved and could aid in the experimental design and control of the underlying mechanisms involved. As a case in point, a recent experimental report incorporating polymer breakage puts forward the intriguing hypothesis that mechanical forces can act as a *selection pressure* in the competition between replicators.[25] In an even earlier key experiment, hydrodynamic vortex motion was demonstrated to act as an environmental pressure to select one or the other handedness between two otherwise degenerate mirror symmetric supramolecular populations.[26] One of our main aims here is to explore the impact that both mechanically induced breakage in concert with

fiber fusion have on the mirror symmetry breaking and subsequent chiral amplification. An important aspect of this work is that we consider the polymerization process in a closed system and include reversible reaction steps.[20,21] This enables us to explore the possibility of *absolute asymmetric synthesis* in thermodynamically closed systems (closed to matter flow) taking into account the necessary thermodynamic constraints.[27,28] Absolute asymmetric synthesis is the ability of a system to amplify the tiny statistical chiral fluctuations up to observably large enantiomeric excesses.[29] The simulations underscore the special role of binary fusion as a nonlinear mechanism, dynamically akin to autocatalysis, for amplifying the initially tiny chiral perturbations up to final large enantiomeric excesses, and in the *absence* of chiral or mutual inhibition.

Model

The nucleated polymerization network is that of a racemizing monomer pair (L_1, R_1) yielding homochiral chains of a maximum length L_N, R_N, where N is the number of monomer units. Monomers attach reversibly to all size chains of the same chirality. Small length post-critical chains up to a certain maximum length can be incorporated via end-to-end fusion into larger chains of the same chirality. The inverse process, fragmentation of large chains into two smaller chains, is also allowed (see Fig. 1). The rates (see Table 1) of these chain-fusions and fragmentations obey the constraints of chemical thermodynamics. The longest chains, from the maximum length on down to a lower length limit, are subjected to mechanical breakage, which is the only irreversible process in the scheme. This breakage represents an *external energy* input to the system. The microscopic transformations defining our scheme are given

as follows:

$$L_1 \rightleftharpoons R_1 \tag{1}$$

$$L_1 + L_j \rightleftharpoons L_{j+1}, \qquad R_1 + R_j, \rightleftharpoons R_{j+1} \qquad (n_c \leq j \leq N-1), \tag{2}$$

$$L_i + L_j \rightleftharpoons L_n,\ R_i + R_j \rightleftharpoons R_n, (i \leq j, i_{minf} \leq i \leq N - j_{minf}, j_{minf} \leq j \leq N - i_{minf}), \tag{3}$$

$$L_n \rightarrow L_i + L_j, \quad R_n \rightarrow R_i + R_j, \qquad (n_{min} \leq n \leq N,\ i_{min} \leq i,\ i \leq j). \tag{4}$$

The racemization, Eq. (1), proceeds with rate k_r, and the stepwise monomer attachment, Eq. (2), with forward/reverse rates k_1, k_{-1} and k_2, k_{-2}, in the nucleation and elongation phases, respectively. The fusion of chains of lengths i and j to a polymer of length $n = i + j$, Eq. (3), occurs with forward/reverse rates k_a, k_{-a} and the irreversible breakage of polymers of length n into polymers of lengths i and j, Eq. (4), with rate γ. The processes are defined to occur over various regions or chain length intervals, as indicated. We consider both the critical nucleus size n_c and maximum chain length N to be fixed, then we need only specify four independent size limits: $n_{min}, i_{min}, i_{minf}$ and j_{minf}; see Table 1 for a summary of their definitions and Fig. 1 for a schematic diagram of the mechanical breakage and fusion processes. The transcription of the scheme's processes Eq. (1-4) into the corresponding differential rate equations leads to *generalized* Smoluchowski equations. Such equations play an important role in reversible polymerization processes and in related aggregation and fragmentation processes.[30–35] In our model, the variable window sizes for the chain fusion/fragmentation processes and for the irreversible mechanical breakage of chains imposes somewhat intricate constraints on the corresponding fusion/fragmentation and breakage kernels which must be accounted for correctly as many detailed features, revealed by the subsequent numerical simulations, depend non-linearly on these window sizes themselves. The details of how these window size constraints are handled are explained in the Appendix.

The model in Eqs. (1-4) is left-right symmetric, that is, possesses a discrete Z_2 symmetry, all species are interchanged with their mirror image counterpart, which is manifest

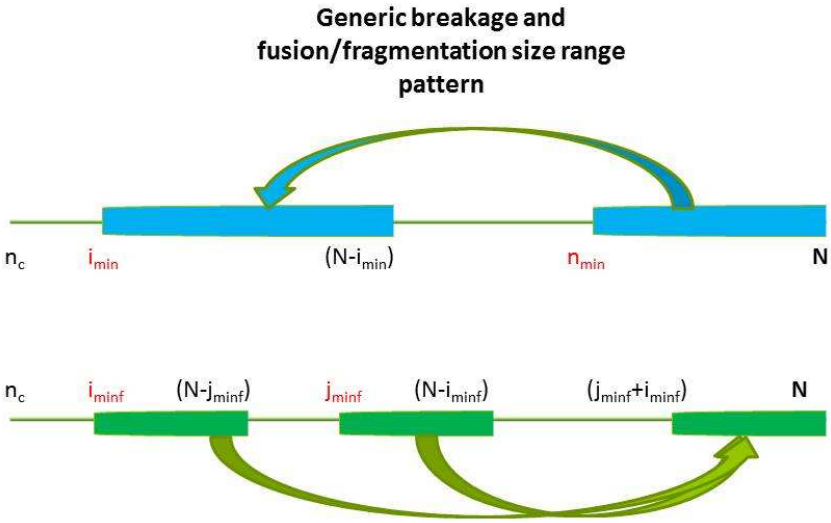

Figure 1: Schematic of the oligomer length ranges involved in the mechanically induced irreversible breakage (upper diagram) and reversible binary end-to-end fusion (lower diagram). N and n_c denote the maximum length polymer and the size of the critical nucleus, respectively, both taken as fixed. Then the breakage pattern is fully determined by $n_{min} \leq N$: the minimum length polymer subject to mechanical breakage and $i_{min} \geq n_c$: the smallest length polymer fragment resulting from this breakage and such that $[\frac{n_{min}}{2}] > (i_{min} - 1)$. The binary fusion pattern is fully determined by $i_{minf} \geq n_c$: the minimum length of the shorter polymers that can fuse with the longer ones, and $j_{minf} \geq i_{minf}$: the minimum length of the longer polymers that can fuse with the shorter ones. Depending on the values for i_{min}, n_{min} and i_{minf}, j_{minf}, the breakage source and breakage product size intervals can overlap; and the fusion source and fusion product size intervals can overlap. There can also be overlap between the various breakage and fusion size ranges. See also Table 1.

in the elementary reaction steps, in the rate constants (Table 1), and in the corresponding differential rate equations [Eq. (36) in the Appendix]. This exact symmetry can be broken spontaneously by the dynamical solutions of the differential rate equations. The model is thus apt for investigating spontaneous mirror symmetry breaking. Rate-equation theory as employed in chemical kinetics is used to describe the differential rate equations of the reaction network. Due to the variable size ranges involved, it is convenient to consider the specific processes (nucleation + racemization + linear chain growth, mechanical breakage,

Table 1: Definition of the model parameters. Above the solid line: the independent parameters. Below the line: the dependent parameters. Length refers to the number of monomer units in the oligomer. Compare with Fig. 1 indicating the various size ranges implied by the different processes. For the overall free energy profile for cooperative nucleated supramolecular polymerization, see, e.g., the schematic diagram Fig. 24 of Ref.[36] The rate constants k_2, k_{-2} and k_a, k_{-a} obey a thermodynamic constraint, see the Appendix. We treat cooperative nucleated polymerization as $k_1 < k_{-1}$, $k_2 > k_{-2}$. Parameters and variables are in standard SI units.

n_c	critical nucleus ($n_c \geq 2$) for cooperative nucleated polymerization
N	maximum length polymer
n_{min}	minimum length polymer subject to mechanical breakage
i_{min}	smallest length polymer fragment resulting from mechanical breakage
i_{minf}	minimum length of the shorter polymers that can fuse with the long polymers
j_{minf}	minimum length of the longer polymers that can fuse with the short polymers
γ	rate of irreversible mechanical breakage of the polymers
k_1, k_{-1}	forward, reverse rates of monomer addition (isodesmic nucleation regime)
k_2, k_{-2}	forward, reverse rates of monomer addition (isodesmic elongation regime)
k_a, k_{-a}	rate of chain-chain fusion, rate of binary fragmentation
k_r	racemization rate of the monomers
$c_k^{L,R}(t)$	time dependent concentration of the k-mer, for chirality L, R
$N - i_{min}$	maximum length breakage fragment
$N - j_{minf}$	maximum length of the shorter polymers that can fuse with the long polymers
$N - i_{minf}$	maximum length of the longer polymers that can fuse with the short polymers
$i_{minf} + j_{minf}$	minimum length of polymers formed by binary fusion

fusion/fragmentation) individually and how they lead to generalized Smoluchowski equations in the Appendix. The isodesmic approximation[36] for the elongation phase of the polymerization leads to an important thermodynamic constraint relating stepwise growth and chain fusion which we derive in the Appendix.

Numerical Methods

As mentioned earlier, we are interested in testing the model's ability to amplify the initial small statistical deviations about the idealized racemic composition,[37,38] in systems closed to matter flow, and taking microscopic reversibility and the thermodynamic constraints into account. The differential rate equations, Eq. (36) from the Appendix, were numerically integrated with the version 10 Mathematica environment[39] and using a high level of nu-

merical precision, typically thirty significant digits, to ensure the numerical significance of the initial concentrations and enantiomeric excesses employed. The results were monitored and verified to assure that total system mass remained constant in time. See[40] for further remarks concerning the numerical integration method options and the numerical precisions used for suppressing the computational noise below the level of the initial chiral fluctuations. The concentration units are $\mathrm{mol}\, L^{-1}$, and the different reaction rate constants have the appropriate units to yield rate values in units of $\mathrm{mol}\, s^{-1}$.

The initial percent enantiomeric excess $ee_0(\%)$ for the system is defined as

$$ee_0(\%) = \frac{\sum_{n=1}^{N}([L_n]_0 - [R_n]_0)}{\sum_{n=1}^{N}([L_n]_0 + [R_n]_0)} \times 100. \tag{5}$$

In order to study the sensitivity of the reaction scheme, Eqs. (1-4), to tiny initial enantiomeric excesses, an initial concentration of a scalemic (non racemic) monomer composition was employed in the calculations: these initial monomeric concentrations are $[L_1]_0 = (0.1 + 1 \times 10^{-11})M$ and $[R_1]_0 = 0.1M$. The maximum polymer length was fixed to $N = 100$, and the critical nucleus size to $n_c = 5$. The full set of the remaining initial concentrations are as follows: $[L_n]_0 = [R_n]_0 = 0.1M$, $2 \leq n \leq N$, i.e., the racemic composition for the remainder of the oligomers (and at a level of numerical working precision that ensures the significance of the initial enantiomeric excess). Inserting these initial concentration values into Eq.(5) yields an initial percent chiral excess of $ee_0 = 5 \times 10^{-11}$ %. While this may seem rather small, it is two orders of magnitude greater than the expected enantiomeric excess due to purely statistical fluctuations in a racemic sample:[37]

$$ee_{stat} = \frac{0.68(\%)}{\sqrt{M}} = 2.0 \times 10^{-13}\%, \tag{6}$$

where $M = 12 \times 10^{24}$ is the total number of oligomers in the system (Avogadro's number multiplied by the total initial concentration of the system).

Values of the reaction rate constants used in all the simulations are: $k_1 = 10^4, k_{-1} = 4 \times$

$10^4, k_2 = 1000, k_{-2} = 900, k_a = 10, k_{-a} = 9, k_R = 10^2, \gamma = 50$. Note the forward and reverse rates of monomer attachment (k_2, k_{-2}) and those of binary fusion (k_a, k_{-a}) are constrained by chemical thermodynamics, see the Appendix for the derivation of this important constraint. The upper and lower limits for the breakage and fusion source and product size windows are specified in the corresponding simulation figure captions. In all the numerical simulations, the character of the final stationary state was inferred from the constant final concentration values for all species maintained during long time intervals ($\approx 10^{15} s$).

Results and Discussion

Results are quantified in terms of standard chiral measures. The percent enantiomeric excess values of the homochiral oligomers are calculated according to $(1 \leq n \leq N)$:

$$ee_n(\%) = \frac{[L_n] - [R_n]}{[L_n] + [R_n]} \times 100. \tag{7}$$

The importance of the enantiomeric excess is that it is an order parameter for the symmetry breaking transition: $|ee_n(\%)| \geq 0$ is strictly zero for mirror symmetric states and nonzero otherwise. In the latter case, the Z_2 symmetry is broken. A distinct global measure of the degree of symmetry breaking is provided by the total mass within each chiral population η_L, η_R:

$$\eta_L = \sum_{n=1}^{N} n[L_n], \qquad \eta_R = \sum_{n=1}^{N} n[R_n], \tag{8}$$

as well as the total chiral mass: $\eta_{Total} = \eta_L + \eta_R$. It is important to keep in mind that $ee_n(t), \eta_L(t), \eta_R(t)$ are all time-dependent quantities.

The outcomes of the numerical calculations are presented in various figures for a selection of breakage and fusion window sizes and are also summarized by phase diagrams indicating the parameter ranges where mirror symmetry is broken in relation to the various size intervals over which the processes of mechanical breakage and fusion/fragmentation are acting. There,

n_{min} represents the lower bound for the longest polymers susceptible to breakage into two fragments whereas i_{min} is the minimum length fragment (see Table 1). Then, $N - i_{min}$ is the upper bound on the fragment size thus generated. The positivity condition on the breakage rate, $[\frac{n_{min}}{2}] > (i_{min} - 1)$, implies a lower limit on n_{min} for a given i_{min}, as indicated in the phase diagrams ([..] indicates the Floor function). On the other hand, binary fusion is a quadratic process, hence the size intervals of the two polymers that fuse together must be specified: these are uniquely determined by i_{minf}, the lower bound on the smaller polymers that can fuse with the typically larger polymers of minimum length $j_{minf} \geq i_{minf}$. Then $N - j_{minf}$ and $N - i_{minf}$ are the upper bounds on the lengths of the smaller, larger polymers that participate in the fusion, respectively. Finally, the size range of the product polymers obtained by this fusion is given by the interval $[j_{minf} + i_{minf}, N]$. Note that all three size intervals have identical width: $\Delta = N - (j_{minf} + i_{minf})$. We consider breakage and fusion to act over the elongation regime of nucleated polymerization, so that the critical nucleus $n_c \leq i_{min} \leq i_{minf} \leq j_{minf}$ sets the strict lower size limit for all these processes. It is clear we must choose $n_{min} \leq N$ and $i_{minf} + j_{minf} \leq N$. There remains substantial freedom in choosing the lower limits of the various size intervals, giving rise to various partial or total process overlap patterns, some of which are indicated below. For instance, we can consider (partial or total) size interval overlap within a given process, say, fusion reactants with fusion products, as well as size range overlap between fusion and breakage size intervals.

A characteristic illustrative example of initial racemic (subject to a tiny chiral perturbation) to the chiral final state transition is shown in Fig. 2 for the ranges of fusion and breakage size limits $i_{minf} = 20, j_{minf} = 30, n_{min} = 85$ and $i_{min} = 25$. Panel (a) shows the time-dependent oligomer enantiomeric excesses, Eq. (7), for all the species collectively. The dependence on the size n of the n-mer: where $1 \leq n \leq N$ indicates that the ee_n depends strongly on the size of the oligomer. The important aspect to be appreciated from panel(a) is the *gradient* in ee_n versus oligomer size n after mirror symmetry is broken and that all the $ee_n > 0$ are *positive*. Since a total of 100 individual curves are plotted together, there

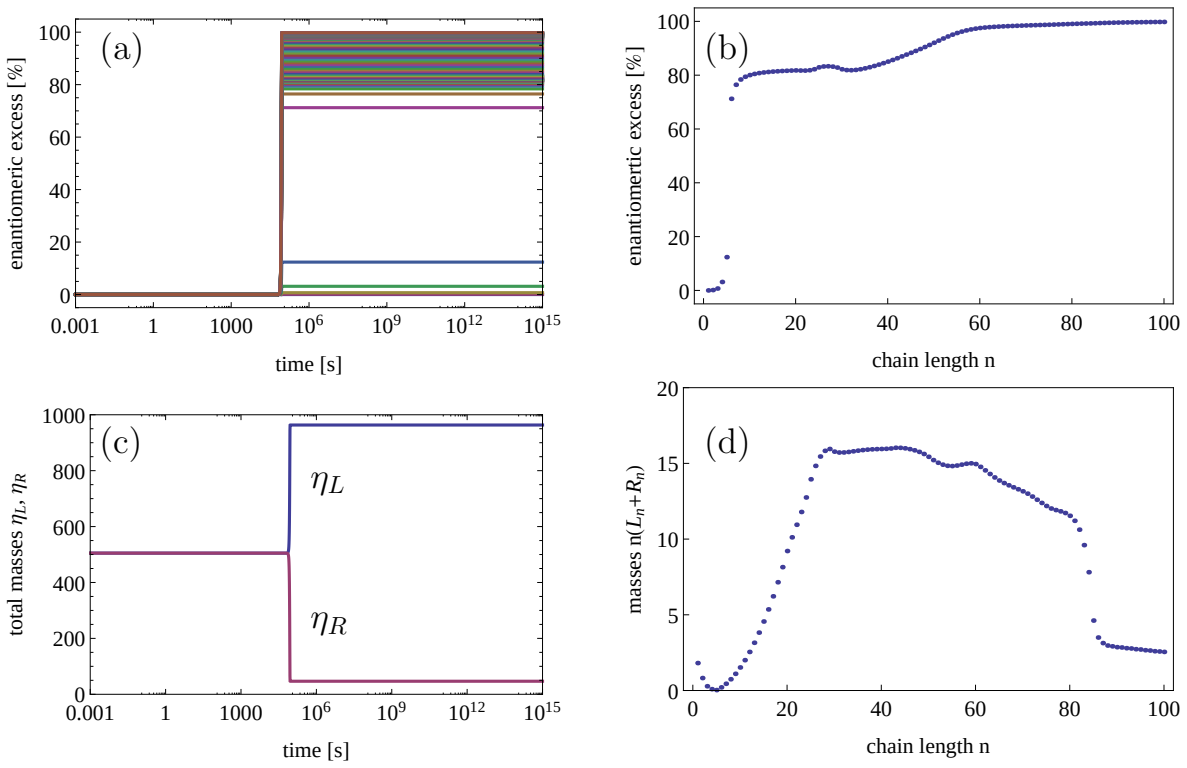

Figure 2: Simulation for $i_{minf} = 20, j_{minf} = 30, n_{min} = 85$ and $i_{min} = 25$. (a) Time-dependent oligomer enantiomeric excess Eq. (7) showing the gradient dependence of ee_n on the size n of the oligomer: the curves correspond to $n = 1$ (bottommost) to $n = 100$ (topmost) and in increasing sequential order. (b) This gradient in n is resolved showing individual oligomer enantiomeric excesses as a function of chain size n and evaluated at $t \sim 10^{15}$s. (c) Total mass in each chiral population Eq. (8) as a function of time. (d) Total chiral mass η_{Total} as a function of chain length n evaluated at $t \sim 10^{15}$s. Time is measured in seconds, concentrations and masses are in standard SI units, as for the remainder of this article.

is a "pile-up" of curves for chain sizes with $n > 6$. This explicit size dependence in ee_n is resolved in the top right hand graph, panel(b), indicating the each oligomer enantiomeric excess as a function of chain size n, evaluated at asymptotic times $t \sim 10^{15}s$. That is, panel (b) results from taking a temporal "slice" of panel (a) after the symmetry breaking event. We see that the gradient in oligomer size is nonlinear. The mirror symmetry breaking is also manifested in the dynamics of the net mass contained within each chiral population (η_L, η_R), Eq. (8), (panel (c)). The way the total chiral mass η_{Total}, summed over both chiral populations is distributed as a function of chain length n, in the complex nonlinear manner,

is shown in panel (d) and evaluated at $t \sim 10^{15}s$. Note that the individual oligomer enantiomeric excesses, panel(a), all exhibit a sigmoidal time dependence. Since this is plotted in a logarithmic scale, the symmetry breaking transition appears abruptly. We can resolve this transition making the sigmoidal character manifest using a linear time scale (see Figures 5,6). The characteristic time scale in which the rapid acceleration phase begins depends on the rate of racemization k_r. Increasing (decreasing) k_r decreases (increases) this time scale. The time dependence of the mass in each chiral species also display sigmoidal behavior (panel (c)), as does the net mass contained within each chiral population for the majority chirality (in this case, for L). The minority enantiomers have their masses correspondingly diminished, in an "anti-sigmoidal" fashion: there is a rapid *deceleration* phase which exactly mirrors the acceleration phase of the majority enantiomers, followed by a rapid slowdown (panel (c)). This chiral "mass splitting" feature, whereby the initial mass degeneracy $[L_n]_0 = [R_n]_0$ (which implies $\eta_L(0) = \eta_R(0)$) is lifted for *all* the species, and on the *same* time scale, is a hallmark feature of spontaneous mirror symmetry breaking (SMSB) in chiral polymerization schemes. Varying the upper and lower size limits of the fusion and breakage windows can lead to similar results as far as the overall qualitative collective symmetry breaking features are concerned. Thus for example in Fig. 3: $i_{minf} = 6, j_{minf} = 80, n_{min} = 95$ and $i_{min} = 20$, (a) exhibits the set of time-dependent oligomer enantiomeric excesses which is similar (but not identical) to the corresponding graph in Fig. 2. As before, the important aspect to be appreciated from panel(a) is the gradient in ee_n versus oligomer size n after mirror symmetry is broken and that all the $ee_n > 0$ are *positive*. In contrast to Figure 2 the "clustering" of the curves is pronounced for the mid-range of the larger sized oligomers. The detailed resolution of the way these ee's are distributed according to chain length (b) reveals a markedly different pattern as compared to the corresponding panel (b) in Fig. 2. This also shows that the mid-range clustering of curves is taking place for oligomers in the size range from approximately $n = 20$ to $n = 80$. This shows that the distribution depends sensitively on the fusion and breakage window size boundaries. Likewise, while the overall

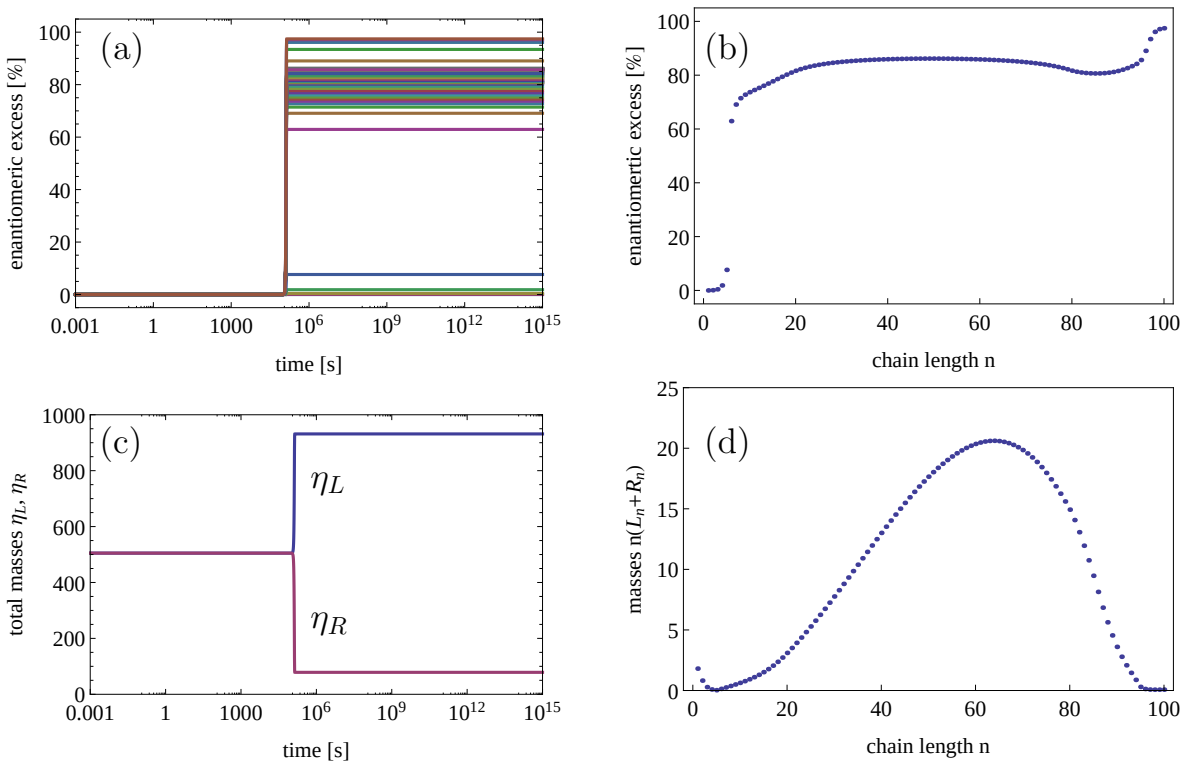

Figure 3: Simulation for $i_{minf} = 6, j_{minf} = 80, n_{min} = 95$ and $i_{min} = 20$. (a) Time-dependent oligomer enantiomeric excess Eq. (7) showing the gradient dependence of ee_n on the size n of the oligomer: the curves correspond to $n = 1$ (bottommost) to $n = 100$ (topmost) and in increasing sequential order. (b) This gradient is resolved showing individual oligomer enantiomeric excesses as a function of chain size n and evaluated at $t \sim 10^{15}$s. (c) Total mass in each chiral population Eq. (8) as a function of time (in seconds). (d) Total chiral mass η_{Total} as a function of chain length n evaluated at $t \sim 10^{15}$s.

sigmoidal time dependence of the total mass in each chiral population is similar for both panels (c) in Figs. 3 and 2, the way in which the total chiral mass is distributed over the chains is radically distinct, see panel (d), again pointing to a clear dependence on the size range over which fusion and breakage are operative.

A further example illustrating the the non-linear dependence on the window sizes is provided in Fig. 4: $i_{minf} = 6, j_{minf} = 6, n_{min} = 100$ and $i_{min} = 50$. In contrast to the previous Figures 2,3 the tight "clustering" of the individual oligomer enantiomeric excess curves is here pronounced for the entire range of the oligomers sizes greater than the critical nucleus. The detailed resolution of the way these ee's are distributed according to chain length (b) con-

firms this aspect unambiguously. Again the overall qualitative aspects of both the collective set of time-dependent oligomer enantiomeric excesses ee_n and the asymptotic chiral masses [Fig. 4(a,c)] are similar to those corresponding to the previous examples. The salient differences are made clear by examining the details of the precise manner in which the oligomer ee_n's and chiral masses are distributed over the individual chain lengths [Fig. 4(b,d)].

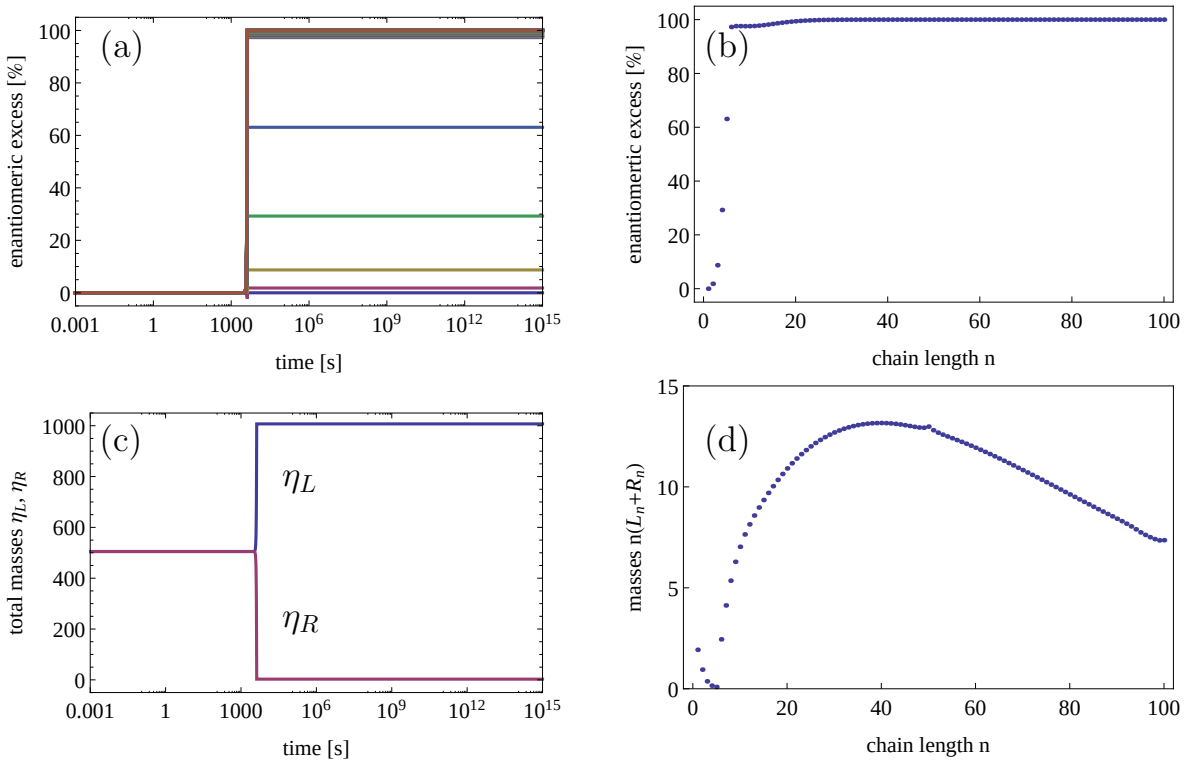

Figure 4: Simulation for $i_{minf} = 6, j_{minf} = 6, n_{min} = 100$ and $i_{min} = 50$. (a) Time-dependent oligomer enantiomeric excess Eq. (7) showing the gradient dependence of ee_n on the size n of the oligomer: the curves correspond to $n = 1$ (bottommost) to $n = 100$ (topmost) and in increasing sequential order. (b) This gradient is resolved showing individual oligomer enantiomeric excesses as a function of chain size n and evaluated at $t \sim 10^{15}$s. (c) Total mass in each chiral population Eq. (8) as a function of time (in seconds). (d) Total chiral mass η_{Total} as a function of chain length n evaluated at $t \sim 10^{15}$s.

The results shown in Figs. 2-4 lead to an important observation. Namely, when SMSB and chiral amplification occur, they are a *collective* and *coherent* phenomena, affecting all of the species and on the same time scale, and such that the symmetry breaking experienced in each individual chiral species (oligomer) is produced with the same sign ($n \in [1, N]$): that

is, the SMSB is homochiral. Employing a logarithmic time scale to display the results in the panels (a),(c) of the above figures affords a compact and concise way to appreciate the collective behavior of all the oligomer enantiomeric excesses in a glance, as well as the total chiral masses, over the entire time range of the simulations. The familiar sigmoidal response of the oligomer enantiomeric excesses can be brought out easily by "zooming" in on the transition time scale using a linear time scale. Thus, for the same simulation parameters leading to Fig. 2, we expose this sigmoidal behavior for the individual oligomer concentrations as well as for the oligomer masses: see panels (a) of Fig. 5 and Fig. 6, respectively. Since we have to deal with 100 species, for clarity we plot a selection of oligomer sizes as shown. It is clear from these curves that the ee_n of the majority enantiomers follow a sigmoid, whereas the minority enantiomers follow an anti-sigmoid (i.e., having a rapid deceleration phase). We note moreover the chiral splittings all take place on a similar time scale for all the oligomers, also the saturation phase (leveling off of curves) occurring on a similar time scale for all the oligomers. In panel (b) of Fig. 5 we expose the sigmoidal behavior in terms of the chiral concentrations and also in terms of the total chiral masses in panel (b) of Fig. 6. The latter should be compared to panel (c) of Fig. 2. An indication of the polymeric relaxation processes taking place before and after the symmetry breaking event is provided by the panels (c),(d) of Fig. 5 and in terms of the oligomer concentrations. The panel (c) shows the individual oligomer concentrations over the full size range in n. The distribution at $t = 10^4 s$, is racemic, at $t = 10^6 s$, the distributions of all the L and R oligomers have separated as shown (and maintain these profiles for the remainder of the simulation). Panel (d) shows the total chiral distribution in terms of the concentrations ($[L_n] + [R_n]$) as a function of oligomer sizes, and for the same two time scales. The sigmoidal response and relaxation processes are also monitored in terms of the chiral masses of the oligomers in Fig. 6.

SMSB results qualitatively similar to those in Figs. 2-4 have been obtained and verified in case-by-case simulations for many other choices of the breakage and fusion window bounds. Among all possible allowed choices of $i_{minf}, j_{minf}, n_{min}$ and i_{min}, a small but illustrative set

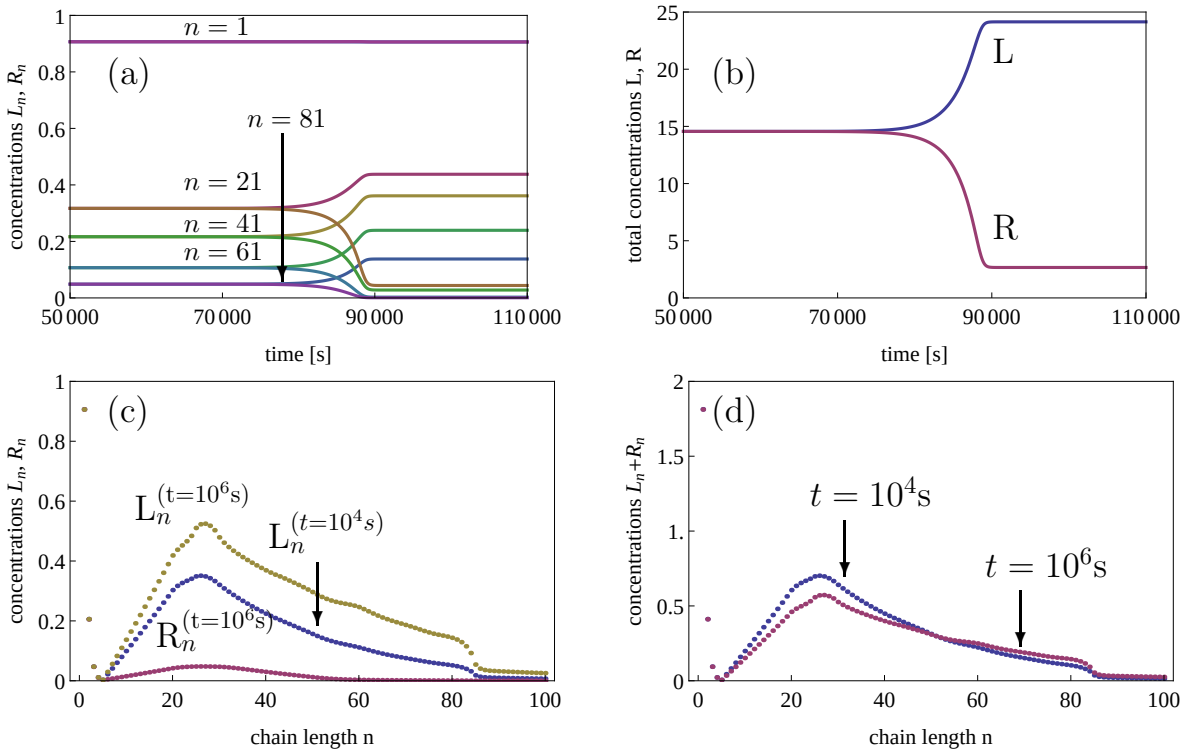

Figure 5: Details of the behavior of the oligomer concentrations: same parameters as for simulation of Fig. 2. (a) Time-dependent oligomer concentrations $[L_n]$ (monotonic increase) and $[R_n]$ (monotonic decrease) for the oligomers with length $n = 1, 21, 41, 61, 81$ showing a close-up of the sigmoidal behavior on a linear time scale (in seconds). (b) Sigmoidal behavior of the total chiral concentrations $\mathrm{L} = \sum_{n=1}^{100}[L_n]$ (monotonic increase) and $\mathrm{R} = \sum_{n=1}^{100}[R_n]$ (monotonic decrease) as functions of time in seconds (linear scale). (c) Individual oligomer concentrations $1 \leq i \leq 100$, before ($t = 10^4$s) and after ($t = 10^6$s) the symmetry breaking. (d) Sum of the chiral concentrations $[L_n] + [R_n]$, as a function of chain length n evaluated before ($t = 10^4$s) and after ($t = 10^6$s) the symmetry breaking.

of so-called "extreme" cases is worth mentioning first. The choice (i) $i_{minf} = 6, j_{minf} = 6, n_{min} = 12$ and $i_{min} = 6$ corresponds to the maximal overlap between the range of the large polymers subject to breakage and the "fallout" range populated by the breakage products. At the same time, this implies a maximal overlap between the ranges of the small and large polymers that can fuse with the range of the fusion products. In addition, both the breakage and fusion windows overlap identically. This is because $i_{min} = i_{minf} = j_{minf} = 6$, $n_{min} = (i_{minf} + j_{minf}) = 12$ and $(N - i_{min}) = (N - i_{minf}) = (N - j_{minf}) = 94$ (to see that the corresponding range overlaps, substitute these window bounds into Fig. 1). In this

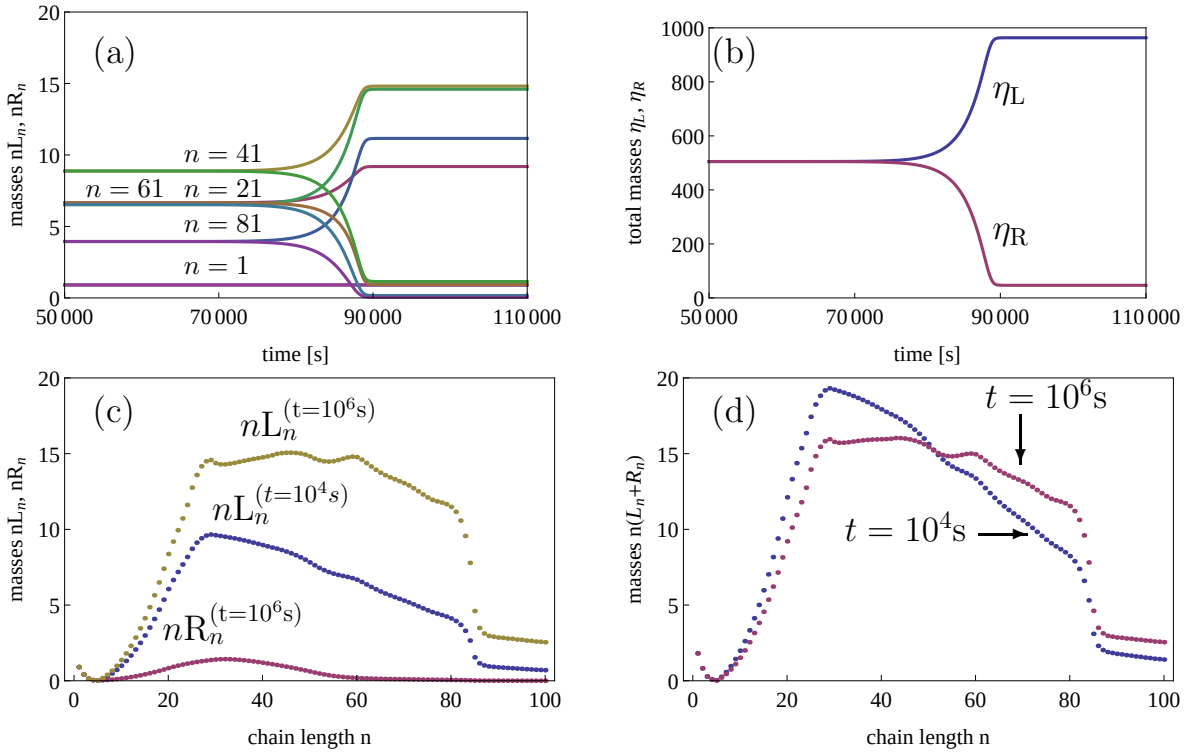

Figure 6: Details of the behavior of the oligomer masses: same parameters as for simulation of Fig. 2. (a) Time-dependent oligomer masses $n[L_n]$ (monotonic increase) and $n[R_n]$ (monotonic decrease) for the oligomers with length $n = 1, 21, 41, 61, 81$ showing a close-up of the sigmoidal behavior on a linear time scale (in seconds). (b) Sigmoidal behavior of the total chiral masses η_L (monotonic increase) and η_R (monotonic decrease) as functions of time in seconds (linear scale). (c) Individual oligomer masses $n[L_n]$, $n[R_n]$ for $1 \leq i \leq 100$, before ($t = 10^4$s) and after ($t = 10^6$s) the symmetry breaking. (d) Sum of the chiral masses $\eta_L + \eta_R$, as a function of chain length n evaluated before ($t = 10^4$s) and after ($t = 10^6$s) the symmetry breaking.

maximal situation, SMSB occurs. Next, keep the fusion windows bounds maximal as in (i), but now shrink the breakage windows to points according to (ii) $i_{min} = 50$ and $n_{min} = 100$. Then the only polymers that can break are the maximal ones ($N = 100$) and the only fragments produced are each of length 50. The breakage intervals become points, and the overlap between breakage and fusion windows is minimized. In this case, SMSB also results. Next, if we keep the breakage parameters as in the previous case and now shrink the fusion windows according to the choice (iii) $i_{minf} = j_{minf} = 50$, then the racemic outcome is the final stable solution. Lastly, maintaining these same fusion parameters as in (iii), now set

(iv) $n_{min} = 12, i_{min} = 6$ to open the breakage source and product windows maximally. Again, the racemic outcome is the final stable solution. The outcomes of these four extreme cases suggest that the chain fusion mechanism plays a crucial role in SMSB. Indeed, SMSB pertains for both cases (i) and (ii) in which the fusion windows are at their maximum widths; whereas Cases (iii) and (iv) lead to the racemic, for which the fusion windows are at their *minimum* widths. The widths of the breakage windows, whether maximal or minimal, play no decisive role in any of these extreme examples.

A more detailed investigation of the regions in parameter space where spontaneous mirror symmetry breaking takes place can be mapped out using the common lower limit $i_{minf} = j_{minf}$ of the fusion windows as a dependent variable. An example of this mapping is provided by the graph in Fig. 7. The regions where SMSB occurs are "islands" which shrink in size as $i_{minf} = j_{minf}$ increases. Recall that as $i_{minf} = j_{minf}$ increases, the area for which fusion processes are allowed decreases. In particular, as $i_{minf} = j_{minf} > 30$, no SMSB is observed for any combination of n_{min}, i_{min} (for the extreme case $i_{minf} = j_{minf} = 50$ we already noted this above). This confirms that the fusion mechanism must be operative over a sufficiently wide range of chain length sizes in order for SMSB to result. In fact, simulations (not displayed here) show that if we eliminate fusion from the overall scheme ($k_a = k_{-a} = 0$), the asymptotic state is racemic, demonstrating that fusion is a crucial process in spontaneous mirror symmetry breaking.

Additional maps showing the regions where SMSB occurs when the two size range intervals of the smaller and larger fusion sources are widely separated, $i_{minf} < j_{minf}$, are displayed in Fig. 8.

Conclusions

We have elaborated a kinetic reaction scheme demonstrating how spontaneous mirror symmetry breaking (SMSB) can be achieved in enantioselective polymerization without invoking

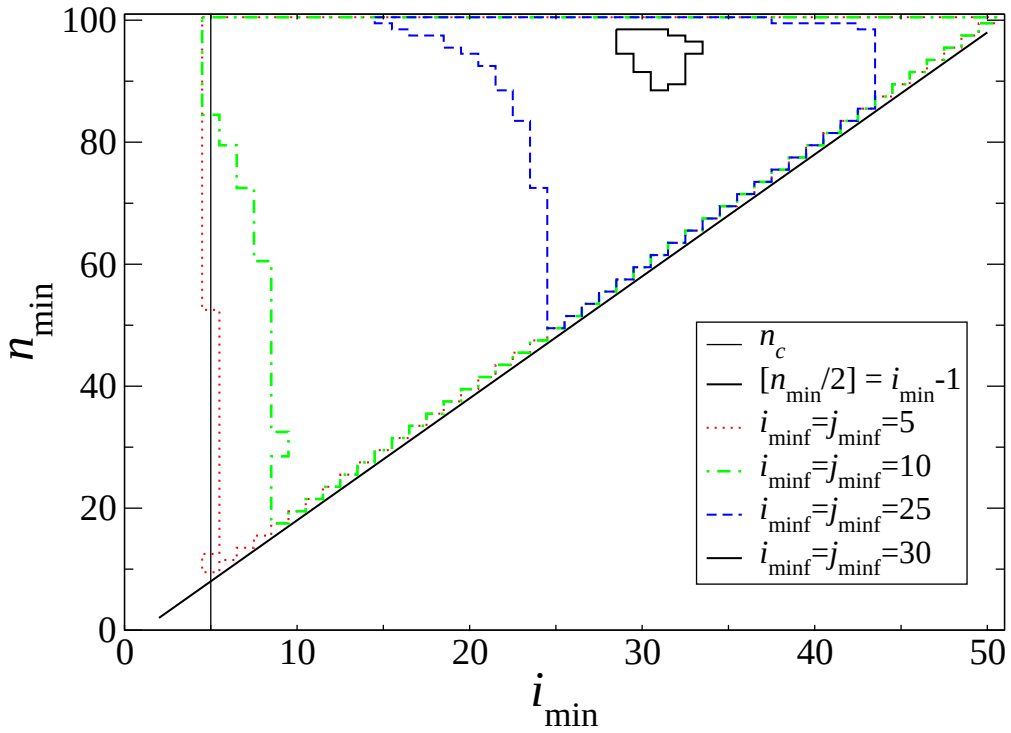

Figure 7: Regions where SMSB is found (within the colored curves) as the common lower bound $i_{minf} = j_{minf}$ of the fusion source size intervals is varied versus n_{min} and i_{min}. This area of the mirror symmetry breaking phase shrinks upon increasing this common lower bound. See also Fig. 1 and Table 1.

the Frank paradigm of mutual or chiral inhibition, in marked contrast to previous chiral polymerization models.[2–7] The model contains the key steps in nucleated cooperative polymerization, i.e., nucleation, elongation, dissociation, fusion and fragmentation. The only way the reaction schemes of the two enantiomers are coupled is through monomer racemization. All these processes are reversible. Fundamental thermodynamics requires that in an isolated system, the asymptotic state is the racemic one. In order to allow a closed system to undergo permanent symmetry breaking, we need an external energy source that here is provided by the irreversible breakage of the longest polymers. Through extensive simulations we show that the fusion process is necessary to induce spontaneous mirror symmetry breaking. The fixing of an upper bound of our polymer length, here $N = 100$, may seem a limitation on

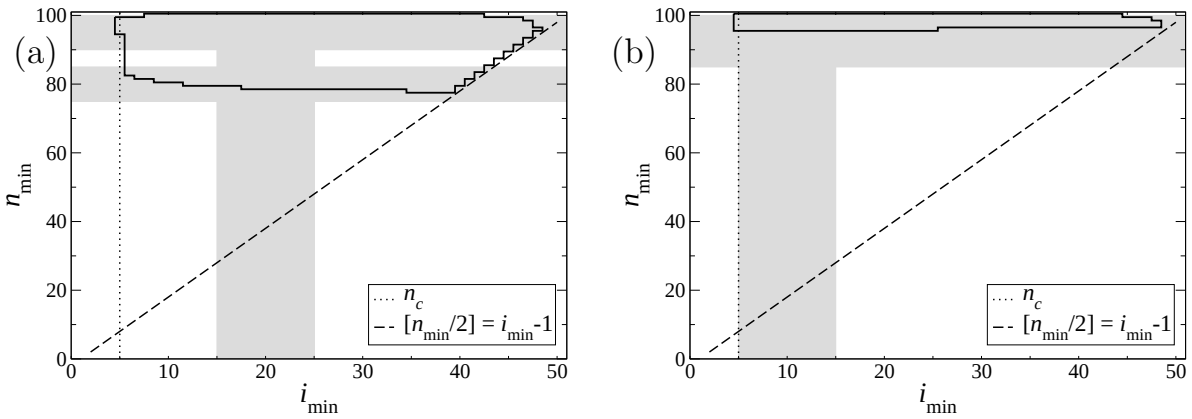

Figure 8: Regions of SMSB (within the area closed by the thick solid curve) as the minimum polymer size n_{min} that can break, and the minimum size fragment i_{min} so generated. Gray shaded bands represent the size interval pattern for the polymers involved in the fusion/fragmentation process. (a) $i_{minf} = 15$ and $j_{minf} = 75$. Thus, since $N = 100$, the length range of the shorter polymers that fuse is $[15, 25]$ (vertical band) with the larger ones $[75, 85]$ (lower horizontal band) whereas the range of the longest product polymers is $[90, 100]$ (upper horizontal band). The width of all three size intervals is $\Delta = 10$. The vertical line at $n_c = 5$ marks the critical nucleus; the diagonal line marks the lower boundary of the (n_{min}, i_{min}) region in which the breakage rate is positive (see text for explanation). See text for initial conditions and rate constants. (b) Same as (a), but for $i_{minf} = 5$ and $j_{minf} = 85$. Thus, since $N = 100$, the length range of the shorter polymers that fuse is $[5, 15]$ (vertical band) with the larger ones $[85, 95]$ whereas the range of the longest product polymers is $[90, 100]$. These two size bands overlap (horizontal band). The width of all three size intervals is $\Delta = 10$.

our model. Nevertheless, this can be justified since polymers cannot grow indefinitely in any case because of mass limitation (finite mass system) and also also due to entropic effects. In many cases, such as exemplified in Figs. 2 and 3, long chains are not generated. So we believe that the system studied here captures the correct qualitative behavior of a putative system where no maximum size N is imposed.

The interest in systems dispensing with mutual inhibition is as follows. In biopolymers, the diastereoselective selection towards homochirality has been confirmed by experimental reports on the polymerization of amino acids and nucleotides from racemic mixtures where, after a certain chain length, the diastereoselective formation of homochiral chains occur preferentially.[13,17,41,42] In light of these results, it is difficult to conceive how such systems, where homochiral interactions dominate, can simultaneously accommodate *heterochiral*

cross inhibition reactions. In this respect, the SMSB mechanism operating in the Viedma deracemization experiment[43] (the grinding of conglomerate racemic mixtures of crystals of achiral or racemizing compounds, in saturated solutions) is radically distinct to both Frank-like and limited enantioselective (LES) reaction schemes exhibiting SMSB. The importance of mechanical grinding for inducing chiral symmetry breaking (and in the context of the Viedma experiment) has inspired subsequent experimental, theoretical and numerical models aimed at achieving a better understanding of attrition-enhanced deracemization.[44–51] A recent kinetic study of the Viedma deracemization phenomenon postulated that the basic transformations responsible for the deracemization of racemic enantiopure crystals could be appropriately extended and applied to model SMSB in enantioselective polymerizations.[29,40] The mechanical breakage (which is an external energy input to the system) of the longer chains is a recycling of lower to higher energy compounds. SMSB occurs due to the competition, established via solution phase racemization of the monomeric units, between these two chiral recyclings. Thus, in the absence of mutual inhibition and other processes, (reversible) binary fusion is a necessary nonlinear process for amplifying the tiny inherent statistical chiral fluctuations, in an otherwise racemic composition of homochiral chains. This being the case, the inclusion of cross-inhibition in our model, would lead to a decrease in the racemic composition of the system and to an increase in the enantiomeric excess value. In other words, a cross-inhibition mechanism has, by itself, a strict deracemizing tendency.[2–7,29] The absence of cross-inhibition in our model thus implies that SMSB and the subsequent amplification to large values of *ee* must rely solely on the purely homochiral processes alone: stepwise growth, fusion/fragmentation and mechanical breakage where each homochiral population is coupled to the population of the opposite chirality via solution phase racemization of the monomers.

As conjectured in,[29,40] the fundamental SMSB *mechanism* underlying Viedma deracemization, i.e., the breakage-fusion recycling, is a process that, when applied to homochiral enantioselective polymerizations, also ought to lead to SMSB. The significance of this with

respect to biological homochirality is that, assuming that the emergence of catalytic functionalities[52] is necessary to convert biopolymer replicators into the hypercyclic replicators, then such an event has a reasonable probability to occur when a large number of different homochiral polymers (composed by different residues) are formed and that very probably homochiral purity is an advantage for the selection. A recent report on chiral hypercycle replicators formed from achiral or racemizing resources shows how they can lead to spontaneous mirror symmetry breaking, without any heterochiral inhibition reactions, such as those of the Frank-like models.[53] Those results indicate that the chemical models for the emergence of primordial autocatalytic self-reproducing systems, of and by themselves, can also explain naturally the emergence of biological homochirality. That work was not concerned with how the homochiral replicators may actually be obtained from either achiral or racemizing resources. This prior SMSB in enantioselective polymerization is then a necessary step for the emergence of chiral hypercyclic replicators. One of the major aims of the present work was to address this issue (the formation of the homochiral polymers themselves), and especially in light of experimental techniques using hydrodynamic shear stresses for breaking up supramolecular structures.[25,26]

The simulations suggest that the key necessary condition for achieving SMSB is the binary chain-fusion mechanism. Indeed, if we delete fusion from the overall scheme ($k_a = k_{-a} = 0$), racemic initial conditions lead to strictly racemic configuration for all time scales, including asymptotic times. It has been argued that autocatalytic processes are at the core of mechanisms that destabilize the racemic state and stabilize the chiral ones.[54] The question then arises if such an autocatalytic mechanism is operative in our specific reaction scheme? On the one hand, inspection of the underlying microscopic reaction scheme, Eqs. (1,2,3,4), reveals no elementary process that can be defined as autocatalytic *per se*, that is, a mechanistic transformation of the type $nX \to mX$ for $m > n$, for which a population of a species X is augmented. Furthermore, the differential rate equations that correspond to the binary fusion process, Eq. (22) in the Appendix, which is the only *nonlinear* transformation in our scheme

involving chains, cannot be cast into the general form $dx_i/dt = k(\boldsymbol{X})x_i^p + f(\boldsymbol{X})$ where x_i is the concentration of the ith-species and the exponent $p > \frac{1}{2}$, and according to the classification of the concepts of autocatalysis,[55] would be the *kinetic signature* of autocatalysis. And this is for the simple reason that a chain of length n can only be the fusion-product of two smaller chains of lengths i, j, respectively, and such that $i + j = n$. On the other hand, it is evidently the dynamic, time-dependent aspect of SMSB where the signature of autocatalysis is to be found.[55] This dynamic signature is observed in the time-dependent curves showing SMSB, such as in Figs. 2-4(a,c). There we find sigmoidal curves for the enantiomeric excesses for all k-mer species, as well as for the total mass in each chiral population: a dynamic signature characterized by a slow initiation phase, then a distinct rapid phase of convex rate acceleration followed by a final rapid slowdown. The dynamic curves for the concentrations of all the individual species $[L_n]$ and $[R_n]$, are also sigmoidal when the mirror symmetry is broken, see Fig. 5, as is the response of the individual oligomer masses $n[L_n]$ and $n[R_n]$, see Fig. 6.

Finally we comment that template-directed ligation of oligomers, such as proposed recently in the RNA world,[56] is a plausible prebiotic mechanism that joins two shorter oligomeric strands into a longer one, and so bears a mechanistic and kinetic resemblance to the chain-fusion process discussed in this work. Hence, we speculate that template directed ligation might act as an effective catalytic step to amplify small initial enantiomeric excesses up to large significant levels. We therefore conjecture that homochirality can be achieved already during the very early stages of prebiotic evolution even from racemic mixtures of nucleotide monomers. While we do not discuss the chemical stability of nucleotides in realistic prebiotic environments, it seems plausible that the system may be maintained out of equilibrium. The mechanical breakage via hydrodynamical shear stresses is only one of many experimentally feasible possibilities for achieving this. This external physical force can be substituted by RNA hydrolysis, or by driving a subset of the reactions by external chemical reagents, by means of an open flow, or else in closed systems with inhomogeneous temperature distribu-

tions, and/or with compartmentalized (spatially segregated) reactions. The mirror symmetry breaking in RNA could occur before the longer compositionally diverse sequences fold into the stable structures, some of which may exhibit catalytic activities. Hence SMSB could occur before the beginning of the RNA world as such, in parallel to other processes in the pre-RNA world such as the formation of modular functional RNA sequences.[57]

Acknowledgement

The authors thank Sijbren Otto and Piotr Nowak for correspondence and discussions of experiments on chiral symmetry breaking with synthetic replicators, and Josep M. Ribó for numerous insightful discussions on SMSB. The research of CB, MS and DH is supported in part by the grant CTQ2013-47401-C2-2-P (MINECO). MS and DH form part of the COST Action CM1304 "*Emergence and Evolution of Complex Chemical Systems*". MS acknowledges a STSM-CM1304-061114-051331 visit to DH's group during 6-17 November 2014. CB is an Otis Williams Postdoctoral Fellow in Bioengineering.

Appendix

Monomer attachment/detachment plus racemization

Here we consider the transformations implied by Eq. (1) and Eq. (2). Stepwise monomer attachment takes place over the entire size range from the dimer to the maximum length polymer minus one ($N-1$); and so covers both the nucleation and elongation phases. The two distinct isodesmic ranges of the free energy profile (see e.g., Fig. 24 of Ref.[36]) suggest dividing the associated rate equations into the four size range groups expressed below, where $\alpha = L$ or R.

$$\dot{c}_k^\alpha(t) = k_1 c_1^\alpha (c_{k-1}^\alpha - c_k^\alpha) + k_{-1}(c_{k+1}^\alpha - c_k^\alpha), \qquad 2 \le k \le n_c - 1, \tag{9}$$

$$\dot{c}_{n_c}^\alpha(t) = k_1 c_1^\alpha c_{n_c-1}^\alpha - k_{-1} c_{n_c}^\alpha - k_2 c_1^\alpha c_{n_c}^\alpha + k_{-2} c_{n_c+1}^\alpha, \qquad k = n_c, \tag{10}$$

$$\dot{c}_k^\alpha(t) = k_2 c_1^\alpha (c_{k-1}^\alpha - c_k^\alpha) + k_{-2}(c_{k+1}^\alpha - c_k^\alpha), \qquad n_c + 1 \le k \le N - 1, \tag{11}$$

$$\dot{c}_N^\alpha(t) = k_2 c_1^\alpha c_{N-1}^\alpha - k_{-2} c_N^\alpha, \qquad (k = N). \tag{12}$$

The monomer dynamics follows rigorously from the conservation of total system mass and solution-phase racemization, and holds independently of the other processes (fusion, fragmentation, mechanical breakage) present in the overall scheme:

$$\dot{c}_1^{L,R}(t) = -\frac{d}{dt}\Big(\sum_{k=2}^{N} k\, c_k^{L,R}(t)\Big) + k_r\big(c_1^{R,L} - c_1^{L,R}\big) \tag{13}$$

$$= -2k_1 (c_1^{L,R})^2 + 2k_{-1} c_2^{L,R} - k_1 \sum_{k=2}^{n_c-1} c_1^{L,R} c_k^{L,R} + k_{-1} \sum_{k=3}^{n_c} c_k^{L,R} - k_2 \sum_{k=n_c}^{N-1} c_1^{L,R} c_k^{L,R}$$

$$+ \; k_{-2} \sum_{k=n_c+1}^{N} c_k^{L,R} + k_r\big(c_1^{R,L} - c_1^{L,R}\big). \tag{14}$$

Irreversible breakage of the longest polymers

We next turn to the process in Eq. (4). The reason for introducing specific length scales over which mechanically induced breakage operates is essentially physical. Thus for example, forces originating by shaking the reaction domain or by the action of stirring rods will be transmitted via hydrodynamic shear stresses and these forces ought to act *preferentially* on the longest chains present. Thus we introduce a minimum chain length $n_{min} \le N$ below which the physical forces no longer have any appreciable effect. On the other hand, the chain fragments so produced should also be larger than a certain minimum size $i_{min} \ge n_c$. The general scenario is depicted in the upper diagram in Fig. 1. As remarked earlier, we consider both n_c and N to be fixed, so these two size intervals: the range of larger "source" polymers

subject to breakage and the "fallout range" populated by the smaller breakage products, are completely specified once n_{min} and i_{min} are chosen. Note that partial overlaps of the source and fallout zones are also possible, depending on the choices of i_{min}, n_{min}. A maximal zone overlap pertains for $i_{min} = n_c$ and $n_{min} = 2(i_{min} - 1)$, allowing for breakage to act over the maximum range of polymer sizes, while the smallest possible breakage fragment corresponds to the critical nucleus.

The general expression for the loss rate of the longest polymers lying within a certain size range due to the mechanical breakage into two smaller chains is (see Fig. 1):

$$\dot{c}_n^{\alpha}(t) = -\frac{1}{2} \sum_{i+j=n;\ i,j \geq i_{min}} \gamma_{i,j} c_n^{\alpha}, \qquad n_{min} \leq n \leq N, \tag{15}$$

$$= -\gamma\big([\frac{n}{2}] - (i_{min} - 1)\big) c_n^{\alpha}, \tag{16}$$

where [..] denotes the Floor function. We assume a constant breakage rate $\gamma_{i,j} = \gamma$ over the indicated range of polymer lengths. The sum (if we omit the factor of one-half) is then carried out over all *distinct* integer partitions of n such that the minimum fragment length is i_{min}; see Table 1. Note furthermore that the condition $[\frac{n}{2}] - (i_{min} - 1) > 0$ will hold for all n provided $[\frac{n_{min}}{2}] > (i_{min} - 1)$. This latter inequality establishes a weak bound relating the lower limit n_{min} for the range of large polymers susceptible to breakage and the lower limit i_{min} of the size range of the smaller polymers populated by the breakage fragments thus generated (see Fig. 1). It is needed simply to ensure that the overall breakage rate is *negative*: the rate of change of the concentration in Eq. (16) must be negative: $\dot{c}_n^{\alpha}(t) < 0$, whereas $\gamma > 0, c_n^{\alpha} \geq 0$.

The general expression for the rate of gain of the shorter polymers due to the incoming

fragments produced by the breakage of the longer polymers is (see Fig. 1)

$$\dot{c}_n^\alpha(t) = + \sum_{j \geq i_{min}}^{N-n} \gamma_{n,j} c_{n+j}^\alpha, \qquad i_{min} \leq n \leq N - i_{min}, \tag{17}$$

$$= \gamma \sum_{k \geq i_{min}+n}^{N} q(k)\, c_k^\alpha \qquad q(k) = \mathrm{IF}[k \geq n_{min}, 1, 0], \tag{18}$$

$$= \gamma \sum_{k=max\{n_{min}, n+i_{min}\}}^{N} \left(1 + \delta_{k,2n}\right) c_k^\alpha. \tag{19}$$

We implement the indicated IF function via the lower limits in the final summation. Finally, we must account for the breakage of those long polymers $k = 2n$ that have exactly twice the length of the shorter polymers (stoichiometry).

Fusion of short with long polymers and fragmentation

We next discuss fusion and fragmentation of the chains, as in Eq. (3). Consider first the contributions to the overall set of rate equations due to binary annealing or fusion of short with long polymers. Then, we compute the contributions due to binary fragmentation of the chains, treating fragmentation as the inverse process to fusion. Note: we herein employ the term breakage to refer to the irreversible breakage (e.g., mechanically induced breakage), and fragmentation to refer to the inverse process of fusion.

The general fusion/fragmentation scenario is depicted graphically in the lower diagram in Fig. 1. As before, we consider both n_c and N to be fixed, so the three size intervals implied by binary fusion are: (i) the range of the smaller and (ii) the larger polymers subject to fusion as well as (iii) the range of the resultant largest chains are completely specified once the lower limits i_{minf} and j_{minf} are chosen. We remark that a few qualitatively distinct zone overlap patterns are possible within this scheme. For example, we can have a partial overlap of the zone of the large polymers that fuse, with the zone of the largest fusion-product polymers by lowering i_{minf} and increasing j_{minf}. Then the zone of the smallest polymers that can fuse

is well separated from the latter two. In the other extreme, we can have a maximal overlap of all three zones by simply letting $i_{minf} = j_{minf} = n_c$. This latter situation corresponds to fusion and fragmentation acting over the widest size ranges possible. We note that in all cases all three size intervals have the same width $\Delta = N - (i_{minf} + j_{minf})$.

Binary fusion of chains

We divide the polymer sizes n into a "small" $n \in (i_{minf}, N - j_{minf})$ and "large" $n \in (j_{minf}, N - i_{minf})$ groups. Then, the rate of loss to the small polymers is given by

$$\dot{c}_n^\alpha(t) = -k_a c_n^\alpha(t) \sum_{i=j_{minf}}^{N-n} c_i^\alpha(t), \qquad i_{minf} \leq n \leq N - j_{minf}. \tag{20}$$

Next, the rate of loss to the large polymers is

$$\dot{c}_n^\alpha(t) = -k_a c_n^\alpha \sum_{i=i_{minf}}^{N-n} c_i^\alpha(t), \qquad j_{minf} \leq n \leq N - i_{minf}. \tag{21}$$

These two expressions are related by the the interchange $i_{minf} \leftrightarrow j_{minf}$ in the corresponding limits and size ranges, and is a symmetry of this model. Lastly, the rate of gain to the largest polymers is

$$\dot{c}_n^\alpha(t) = +k_a \sum_{i=i_{minf}}^{n-j_{minf}} c_i^\alpha(t) c_{n-i}^\alpha(t), \qquad j_{minf} + i_{minf} \leq n \leq N. \tag{22}$$

Binary fragmentation

The rate of gain to the small polymers due to fragmentation of the largest ones is

$$\dot{c}_n^\alpha(t) = k_{-a} \sum_{i=j_{minf}+n}^{N} c_i^\alpha(t), \qquad i_{minf} \leq n \leq N - j_{minf}. \tag{23}$$

The rate of gain to the large polymers due to fragmentation of the largest ones is

$$\dot{c}_n^\alpha(t) = k_{-a} \sum_{i=i_{minf}+n}^{N} c_i^\alpha(t), \qquad j_{minf} \le n \le N - i_{minf}. \tag{24}$$

Note that these two expressions are related by the interchange symmetry $i_{minf} \leftrightarrow j_{minf}$ in the summation limits and size ranges.

The rate of loss to the largest polymers due to their very own fragmentation is given by:

$$\begin{aligned} \dot{c}_n^\alpha(t) &= -k_{-a} c_n^\alpha(t) \sum_{i=i_{minf}}^{n-j_{minf}} 1, \qquad j_{minf} + i_{minf} \le n \le N, & (25) \\ &= -k_{-a} c_n^\alpha(t)[n - (j_{minf} + i_{minf}) + 1]. & (26) \end{aligned}$$

Lastly, introducing fusion fluxes Ψ (see also (33) below) allows us to write the fusion and fragmentation processes together in a more compact form:

$$\begin{aligned} \dot{c}_n^\alpha(t) &= -\sum_{i=j_{minf}}^{N-n} \Psi_{n,i}^\alpha(t), \qquad i_{minf} \le n \le N - j_{minf}, & (27) \\ \dot{c}_n^\alpha(t) &= -\sum_{i=i_{minf}}^{N-n} \Psi_{n,i}^\alpha(t), \qquad j_{minf} \le n \le N - i_{minf}, & (28) \\ \dot{c}_n^\alpha(t) &= +\sum_{i=i_{minf}}^{n-j_{minf}} \Psi_{i,n-i}^\alpha(t), \qquad j_{minf} + i_{minf} \le n \le N. & (29) \end{aligned}$$

Assembly of final equations

The complete set of rate equations taking into account all the above processes can be expressed in terms of reaction rate fluxes and stoichiometric matrices. Introduce the reaction

rate fluxes:

$$\phi_j^\alpha = \begin{cases} k_1 c_1^\alpha c_j^\alpha - k_{-1} c_{j+1}^\alpha, & 1 \le j \le n_c - 1, \\ k_2 c_1^\alpha c_j^\alpha - k_{-2} c_{j+1}^\alpha, & n_c \le j \le N-1 \end{cases} \tag{30}$$

$$\phi_r^{L,R} = k_r (c_1^R - c_1^L), \tag{31}$$

$$\Phi_k^\alpha = \gamma c_k^\alpha, \tag{32}$$

$$\Psi_{m,n}^\alpha = k_a c_m^\alpha c_n^\alpha - k_{-a} c_{m+n}^\alpha, \tag{33}$$

for linear chain growth (ϕ), racemization (ϕ_r), mechanical breakage (Φ) and fusion (Ψ), respectively. Although the individual fusion fluxes, Eq. (33), depend on two indices m, n, for purposes of counting they can be enumerated in a sequential fashion by imposing, and without loss of generality, that $m \le n$. The number of independent fusion fluxes is calculated to be

$$N_\psi = \sum_{k=i_{minf}}^{N-j_{minf}} \sum_{l=\max(k,j_{minf})}^{N-k} 1, \tag{34}$$

the lower limit of the second summand ensures that the flux $\Psi_{m,n} = \Psi_{n,m}$ is counted just once.

We can group all these fluxes together into a single flux vector:

$$\boldsymbol{f}^\alpha = \big(\{\phi_j^\alpha\}_{j=1}^{N-1}, \phi_r^\alpha, \{\Phi_k^\alpha\}_{k=1}^{N-n_{min}+1}, \{\Psi_m^\alpha\}_{m=1}^{N_\psi}\big). \tag{35}$$

Then the differential rate equations for the i-th species can be written as follows:

$$\frac{dc_i^\alpha(t)}{dt} = \sum_{j=1}^{n_r} S_{i,j} f_j^\alpha, \qquad 1 \le i \le N, \qquad 1 \le j \le n_r \tag{36}$$

and $\boldsymbol{S}$ is the stoichiometric matrix with elements $S_{i,j}$. The sum is over the number n_r of reactions:

$$n_r = 2N - n_{min} + N_\psi + 1. \tag{37}$$

Equations (36) represent the model to be solved numerically.

Thermodynamic constraint for fusion and fragmentation

We establish the thermodynamic constraint relating the kinetic rate constants of polymer growth by (i) stepwise monomer addition and (ii) by chain fusion in the isodesmic approximation for the elongation phase.

The rate constants of forward monomer addition to a chain of length n and reverse detachment (from a chain of length $n+1$) satisfy

$$\frac{k_n}{k_{-(n+1)}} = \exp\Big([\Delta G^0_{n+1} - \Delta G^0_n]/kT\Big) = \exp\Big(\alpha_n/kT\Big), \tag{38}$$

where α_n is the free energy difference between two chains that differ by a single monomer unit. In the isodesmic approximation, this energy difference is independent of the chain length: thus $\alpha_n = \alpha = const$ (see, e.g., Fig. 24 in[36]).

The rate constants for (forward) annealing/fusion of two chains of lengths p and s, respectively, and (the reverse) rate of fragmentation of a chain of length $p+s$ into these two smaller fragments satisfy

$$\frac{k_{p,s}}{k_{-(p+s)}} = \exp\Big([\Delta G^0_{p+s} - \Delta G^0_p - \Delta G^0_s]/kT\Big) = \exp\Big(\beta_{p,s}/kT\Big), \tag{39}$$

where $\beta_{p,s}$ is the free energy difference between the large chain and these two smaller fragments. In the isodesmic approximation this difference is independent of the chain sizes: $\beta_{p,s} = \beta = const$.

Now identify $n+1 = p+s$, that is, we can obtain a given length polymer via two distinct pathways, either by (i) adding one more monomer to a polymer of length n or (ii) by annealing two smaller polymers of lengths p, s, respectively. Then the difference in free

energies between these two distinct pathways is

$$\alpha - \beta = -\Delta G^0_{p+s-1} + \Delta G^0_p + \Delta G^0_s. \tag{40}$$

We can calculate the free energy difference for any size polymer from Eq. (38) which implies the recurrence relation

$$\Delta G^0_{n+1} - \Delta G^0_n = \alpha, \tag{41}$$

$$\Rightarrow \quad \Delta G^0_n = (n-1)\alpha, \tag{42}$$

and substituting this into Eq. (40) implies $\alpha = \beta$, and so from Eqs. (38,39) we find

$$\frac{k_n}{k_{-(n+1)}} = \frac{k_{p,s}}{k_{-(p+s)}}. \tag{43}$$

Since fusion takes place within the isodesmic elongation phase of polymerization, this implies the following constraint on the rate constants (see Table 1):

$$\frac{k_2}{k_{-2}} = \frac{k_a}{k_{-a}}. \tag{44}$$

References

(1) McGuire, B. A.; Carroll, P. B.; Loomis, R. A.; Finneran, I. A.; Jewell, P. R.; Remijan, A. J.; Blake, G. A. Discovery of the interstellar chiral molecule propylene oxide (CH_3CHCH_2O). *Science* **2016**, *352*, 1449–1452.

(2) Sandars, P. G. H. A toy model for the generation of homochirality during polymerization. *Orig. Life Evol. Biosph.* **2003**, *33*, 575–587.

(3) Brandenburg, A.; Multamäki, T. How long can left and right handed life forms coexist? *Int. J. Astrobiol.* **2004**, *3*, 209–219.

(4) Brandenburg, A.; Andersen, A. C.; Höfner, S.; Nilsson, M. Homochiral growth through enantiomeric cross-inhibition. *Orig. Life Evol. Biosph.* **2005**, *35*, 225–241.

(5) Wattis, J. A. D.; Coveney, P. V. Symmetry-breaking in chiral polymerisation. *Orig. Life Evol. Biosph.* **2005**, *35*, 243–273.

(6) Gleiser, M.; Thorarinson, J. Prebiotic homochirality as a critical phenomenon. *Orig. Life Evol. Biosph.* **2006**, *36*, 501–505.

(7) Gleiser, M. Asymmetric spatiotemporal evolution of prebiotic homochirality. *Orig. Life Evol. Biosph.* **2007**, *37*, 235–251.

(8) Frank, F. C. On spontaneous asymmetric synthesis. *Biochim. Biophys. Acta* **1953**, *11*, 459–463.

(9) Saito, Y.; Hyuga, J. Chirality selection in open flow systems and in polymerization. *J. Phys. Soc. Jpn.* **2005**, *74*, 1629.

(10) Toxvaerd, S. Molecular dynamics simulations of isomerization kinetics in condensed fluids. *Phys. Rev. Lett.* **2000**, *85*, 4747.

(11) Ricci, F.; Stillinger, F. H.; Debenedetti, P. G. Creation and persistence of chiral asymmetry in a microscopically reversible molecular model. *J. Phys. Chem. B* **2013**, *117*, 602–614.

(12) Blocher, M.; Hitz, T.; Luisi, P. L. Stereoselectivity in the oligomerization of racemic tryptophan N-Carboxyanhydride (NCA-Trp) as determined by isotope labeling and mass spectrometry. *Helv. Chim. Acta* **2001**, *84*, 842–848.

(13) Hitz, T.; Luisi, P. L. Chiral amplification of oligopeptides in the polymerization of alpha-amino acid N-Carboxyanhydrides in water. *Helv. Chim. Acta* **2003**, *86*, 1423–1434.

(14) Nery, J. G.; Bolbach, G.; Weissbuch, I.; Lahav, M. Generation of oligopeptides with homochiral sequences by topochemical reactions within racemic crystals of Phenylalanine-N-Carboxyanhydride. *Angew. Chem. Int. Ed.* **2003**, *42*, 2157–2161.

(15) Hitz, T. H.; Luisi, P. L. Spontaneous onset of homochirality in oligopeptide chains generated in the polymerization of N-Carboxyanhydride amino acids in water. *Orig. Life Evol. Biosph.* **2004**, *34*, 93–110.

(16) Rubinstein, I.; Eliash, R.; Bolbach, G.; Weissbuch, I.; Lahav, M. Racemic beta sheets in biochirogenesis. *Angew. Chem. Int. Ed.* **2007**, *46*, 3710–3713.

(17) Illos, R. A.; Bisogno, F. R.; Clodic, G.; Bolbach, G.; Weissbuch, I.; Lahav, M. Oligopeptides and copeptides of homochiral sequence, via beta-sheets, from mixtures of racemic alpha-amino acids, in a one-pot reaction in water; relevance to biochirogenesis. *J. Am. Chem. Soc.* **2008**, *130*, 8651–8659.

(18) Rubinstein, I.; Clodic, G.; Bolbach, G.; Weissbuch, I.; Lahav, M. Racemic beta-sheets as templates for the generation of homochiral (isotactic) peptides from aqueous solutions of (RS)-valine or -leucine N-Carboxy-anhydrides: Relevance to biochirogenesis. *Chem. Eur. J.* **2008**, *14*, 10999–11009.

(19) Weissbuch, I.; Illos, R. A.; Bolbach, G.; Lahav, M. Racemic beta-sheets as templates of relevance to the origin of homochirality of peptides: Lessons from crystal chemistry. *Acc. Chem. Res.* **2009**, *42*, 1128–1140.

(20) Blanco, C.; Hochberg, D. Chiral polymerization: symmetry breaking and entropy production in closed systems. *Phys. Chem. Chem. Phys.* **2011**, *13*, 839–849.

(21) Blanco, C.; Hochberg, D. Homochiral oligopeptides by chiral amplification: interpretation of experimental data with a copolymerization model. *Phys. Chem. Chem. Phys.* **2012**, *14*, 2301–2311.

(22) Blanco, C.; Hochberg, D. Induced mirror symmetry breaking via template-controlled copolymerization: theoretical insights. *Chem. Commun.* **2012**, *48*, 3659–3661.

(23) Blanco, C.; Hochberg, D. Models for mirror symmetry breaking via beta-sheet-controlled copolymerization: (i) mass balance and (ii) probabilistic treatment. *J. Phys. Chem. B* **2012**, *116*, 13953–13967.

(24) Crusats, J.; Hochberg, D.; Moyano, A.; Ribó, J. M. Frank model and spontaneous emergence of chirality in closed systems. *Chem. Phys. Chem.* **2009**, *10*, 2123–2131.

(25) Carnall, J. M. A.; Waudby, C. A.; Belenguer, A. M.; Stuart, M. C. A.; Peyralans, J. J.-P.; Otto, S. Mechanosensitive self-replication driven by self-organization. *Science* **2010**, *327*, 1502–1506.

(26) Ribó, J. M.; Crusats, J.; Sagués, F.; Claret, J.; Rubires, R. Chiral sign induction by vortices during the formation of mesophases in stirred solutions. *Science* **2001**, *292*, 2063–2066.

(27) Blackmond, D. G.; Matar, O. K. Re-examination of reversibility in reaction models for the spontaneous emergence of homochirality. *J. Phys. Chem. B* **2008**, *112*, 5098–5104.

(28) Stich, M.; Ribó, J. M.; Blackmond, D. G.; Hochberg, D. Necessary conditions for the emergence of homochirality via autocatalytic self-replication. *J. Chem. Phys.* **2016**, *145*, 074111.

(29) Ribó, J. M.; Blanco, C.; Crusats, J.; El-Hachemi, Z.; Hochberg, D.; Moyano, A. Absolute asymmetric synthesis in enantioselective autocatalytic reaction networks: theoretical games, speculations on chemical evolution and perhaps a synthetic option. *Chem. Eur. J.* **2014**, *20*, 17250–17271.

(30) Blatz, P. J.; Tobolsky, A. V. Note on the kinetics of systems manifesting simultaneous polymerization-depolymerization phenomena. *J. Phys. Chem.* **1945**, *49*, 77–80.

(31) Barrow, J. D. Coagulation with fragmentation. *J. Phys. A* **1981**, *14*, 729.

(32) van Dongen, P. G. J.; Ernst, M. H. Kinetics of reversible polymerization. *J. Stat. Phys.* **1984**, *37*, 301–324.

(33) Hendricks, E. M. Cluster size distributions in equilibrium. *Z. Phys. B* **1984**, *57*, 307–314.

(34) Cohen, R. J.; Benedek, G. Equilibrium and kinetic theory of polymerization and the sol-gel transition. *J. Phys. Chem.* **1982**, *86*, 3696–3714.

(35) Ziff, R. M.; McGrady, E. D. The kinetics of cluster fragmentation and depolymerisation. *J. Phys. A* **1985**, *18*, 3027.

(36) De Greef, T. F. A.; Smulders, M. M. J.; Wolffs, M.; Schenning, A. P. H. J.; Sijbesma, R. P.; Meijer, E. W. Supramolecular polymerization. *Chem. Rev.* **2009**, *109*, 5687–5754.

(37) Mills, W. H. Some aspects of stereochemistry. *J. Chem. Technol. Biotechnol.* **1932**, *51*, 750–759.

(38) Mislow, K. Absolute asymmetric synthesis: a commentary. *Collect. Czech. Chem. Commun.* **2003**, *68*, 849–864.

(39) Wolfram Research, Inc., Mathematica Edition 10. Wolfram Research, Inc., Champaign, Illinois, 2014.

(40) Blanco, C.; Crusats, J.; El-Hachemi, Z.; Moyano, A.; Veintemillas, S.; Hochberg, D.; Ribó, J. M. The Viedma deracemization of racemic conglomerate mixtures as a paradigm of spontaneous mirror symmetry breaking in aggregation and polymerization. *ChemPhysChem* **2013**, *14*, 3982–3993.

(41) Lee, D. H.; Granja, J. R.; Martinez, J. A.; Severin, K.; Reza Ghadiri, M. A self-replicating peptide. *Nature* **1996**, *382*, 525–528.

(42) Sczepanski, J. T.; Joyce, G. F. A cross-chiral RNA polymerase ribozyme. *Nature* **2014**, *515*, 440–442.

(43) Viedma, C. Chiral symmetry breaking during crystallization: Complete chiral purity induced by nonlinear autocatalysis and recycling. *Phys. Rev. Lett.* **2005**, *94*, 065504.

(44) Noorduin, W. L.; Izumi, T.; Millemaggi, A.; Leeman, M.; Meekes, H.; van Enckevort, W. J. P.; Kellogg, R. M.; Kaptein, B.; Vlieg, E.; Blackmond, D. G. Emergence of a single solid chiral state from a nearly racemic amino acid derivative. *J. Am. Chem. Soc.* **2008**, *130*, 1158–1159.

(45) Noorduin, W. L.; van Enckevort, W. J.; Meekes, H.; Kaptein, B.; Kellogg, R. M.; Tully, J. C.; McBride, J. M.; Vlieg, E. The driving mechanims behind attrition-enhanced deracemization. *Angew. Chem. Int. Ed.* **2010**, *49*, 8435–8438.

(46) Hein, J. E.; Cao, B. H.; Viedma, C.; Kellogg, R. M.; Blackmond, D. G. Pasteur's tweezers revisited: on the mechanism of attrition-enhanced deracemization and resolution of chiral conglomerate solids. *J. Am. Chem. Soc.* **2012**, *134*, 12629–12636.

(47) Ricci, F.; Stillinger, F. H.; Debenedetti, P. G. A computational investigation of attrition-enhanced chiral symmetry btreakinmg in conglomerate crystals. *J. Chem. Phys.* **2013**, *139*, 174503.

(48) Iggland, M.; Mazzotti, M. Solid state deracemisation through growth, dissolution and solution-phase racemisation. *Cryst. Eng. Comm.* **2013**, *15*, 2319–2328.

(49) Iggland, M.; Mazzotti, M. A population balance model for chiral resolution via Viedma ripening. *Cryst. Growth Des.* **2011**, *11*, 4611–4622.

(50) Gherase, D.; Conroy, D.; Matar, O. K.; Blackmond, D. G. Experimental and theoretical study of the emergence of single chirality in attrition-enhanced deracemization. *Cryst. Growth Des.* **2014**, *14*, 928–937.

(51) Blanco, C.; Ribó, J. M.; Hochberg, D. Modeling spontaneous chiral symmetry breaking and deracemization phenomena: discrete versus continuum approaches. *Phys. Rev. E* **2015**, *91*, 022801.

(52) Kauffman, S. A. Autocatalytic sets of proteins. *J. Theor. Biol.* **1986**, *119*, 1–24.

(53) Ribó, J. M.; Crusats, J.; El-Hachemi, Z.; Moyano, A.; Hochberg, D. Spontaneous mirror symmetry breaking in heterocatalytically coupled enantioselective replicators. *Chem. Sci.* **2017**, *8*, 763–769.

(54) Plasson, R.; Kondepudi, D. K.; Bersini, H.; Commeyras, A.; Asakura, A. Emergence of homochirality in far-from-equilibrium systems: Mechanisms and role in prebiotic chemistry. *Chirality* **2007**, *19*, 589–600.

(55) Plasson, R.; Brandenburg, A.; Jullien, L.; Bersini, H. Autocatalyses. *J. Phys. Chem. A* **2011**, *115*, 8073–8085.

(56) Derr, J.; Mananpat, M. L.; Rajamani, S.; Leu, K.; Xulvi-Brunet, R.; Joseph, I.; Nowak, M. A.; Chen, I. Prebiotically plausible mechanisms increase compositional diversity of nucleic acid sequences. *Nucleic Acids Res.* **2012**, *40*, 4711–4722.

(57) Briones, C.; Stich, M.; Manrubia, S. C. The dawn of the RNA world: Toward functional complexity through ligation of random RNA oligomers. *RNA* **2009**, *15*, 743–749.

Graphical TOC Entry